Bulletin of the Seismological Society of America, Vol. 72, No. 3, pp. 959-979, June 1982

PEAK ACCELERATION SCALING STUDIES

By David M. Hadley, Donald V. Helmberger, and John A. Orcutt

ABSTRACT

An acceleration time history can be decomposed into a series of operations that transfers energy from each point on the fault to the recording station

$$ACC(t) = S^* R^* E^* Q$$

where S is the source time function, R represents rupture over a finite fault, E is the elastic propagation through the earth, and Q is the path attenuation, assumed to be linear. If these operators were exactly known, a deterministic approach to predicting strong ground motions would be straightforward. For the current study, E was computed from a velocity model that incorporates a stiff sedimentary layer over a southern California crust. A range of realistic rupture velocities have been obtained by other investigators and is incorporated into the simulation. Assumptions of the path averaged attenuation, Q, can be tested by comparing with observational data, as a function of distance, the parameters peak acceleration, and computed M_L. This provides a check on both the high frequency (~ 5 Hz) and long-period (~1 sec) behavior of $E^* Q$. An average crustal shear wave Q_β of 300 is found to be compatible with observational data (M_L = 4.5 to 5.0). Assumptions of S can be avoided by using real sources derived from accelerograms recorded at small epicentral distances (epicentral distance/source depth < 1). Using these operators, accelerograms have been simulated for strike-slip faulting for four magnitudes: 4.5; 5.5; 6.5; and 7.0. The shapes of the derived average peak ground acceleration (PGA) versus distance curves are well described by the simple equation PGA α $[R + C(M)]^{-1.75}$, where R is the closest distance to the fault surface and $C(4.5) = 6$, $C(5.5) = 12$, $C(6.5) = 22$, and $C(7.0) = 36$ km.

Introduction

The seismogram recorded by a strong motion accelerograph represents the accumulative effect of many complex processes that transfer seismic energy from the fault surface to the recording instrument. As the rupture front passes a point on the fault, each particle accelerates, reaches some peak velocity, and finally slows to a stop. As each point accelerates, it radiates seismic energy. Before this elastic energy is recorded at the station, it is filtered in several significant ways. The energy is absorbed by anelastic wave propagation and scattered by heterogeneities. Purely elastic propagation through the earth filters the signal (e.g., Helmberger and Malone, 1975; Heaton and Helmberger, 1978). Finally, interaction with the recording site and the instrument results in further distortions. Each physical process can be represented by a filter or operator. The recorded seismogram can be viewed as a representation of the convolution of each operator.

The operators describing the seismic source, attenuation, and wave propagation can be computed analytically or derived empirically. Provided the various operators are known in sufficient detail, the generation of synthetic time histories is fairly straightforward. Recent computational techniques for deriving synthetic seismograms have proven to be powerful tools for studying earthquake source properties and for determining the details of the earth's structure (e.g., Burdick, 1977; Langston, 1978).

In a recent study of the 1940 Imperial Valley earthquake, Hartzell (1978) found that the main shock seismogram recorded at El Centro could be simulated by the superposition of several of the major aftershocks. Physically this simulation is very attractive. The record for each aftershock is the cumulative result, for a portion of the fault, of all physical processes discussed above. To simulate the main shock requires only fairly simple scaling for moment. The lag time for the superposition of each aftershock record is determined by the progression of the rupture front. Kanamori (1979) has carried this technique further by using regional records from the $M = 6.4$ Borrego Mountain earthquake to simulate rupture along the San Andreas for an $M = 8$ earthquake. Since the Borrego Mountain data were not recorded over the full range of distances and azimuths that would be required to simulate ground motion, some scaling of the observed records was necessary. In particular, as the observed records were primarily surface waves, amplitudes were scaled for distance by $r^{\frac{1}{2}}$. Finally, the amplitudes were corrected for radiation pattern, and the scaled observed records were lagged in time to simulate the rupture process.

The estimation of strong ground motion at short epicentral distances resulting from a large earthquake has also been studied with a simulation technique that relied heavily upon the more extensive data set from smaller earthquakes (Hadley and Helmberger, 1980). These investigators used the accelerograms of a well-recorded smaller earthquake as Green's functions for the elements of a larger fault. However, application of this empirical simulation approach has several limitations. Few earthquakes have been well recorded over the range of distances and on comparable site conditions to define the necessary Green's functions required to simulate a large earthquake. Further, variations in source depth have a significant effect on the transfer functions. Without accelerograms from a range of source depths, the adequacy of the simulations will be suspect.

Within this study, the initial simulation discussed by Hadley and Helmberger (1980) has been extended to explicitly include the effects of a stiff sedimentary structure overlying a realistic crust and the effects of energy release over a range of source depths. This has been accomplished by computing the transfer functions directly from an earth model. Observational constraints, as discussed below, have been used in the development and verification of these functions. The following simulation technique is a hybrid approach as observational accelerograms are used to define the time function radiated from each grid element of the simulated fault. The size of the grid elements are scaled to be comparable with the source dimensions of the recorded earthquake. Scaling of the radiated time function for moment release within each element of the fault and the assumed stochastic character of the rupture process across the grid follow the previous work of Hadley and Helmberger (1980). Within the following sections, each operator utilized to produce the final simulated accelerograms is discussed in detail.

Physical Operators

Crustal response. In a previous study of simulating strong ground motion (Hadley and Helmberger, 1980), the crustal transfer functions utilized were empirical. The data used were recorded on essentially hard rock sites located at epicentral distances ranging from of 5 to 33 km. Recorded accelerograms were scaled only for radiation pattern and hypocentral distance. The advantage of this technique is that real crustal transfer functions and real crustal attenuation are automatically incorporated into the simulation. The disadvantage is that the modeling is only appropriate for

a crust typified by the average of the suite of stations recording the earthquake. In addition, the simulation cannot be extended to distances much beyond the range of the recorded data.

An obvious alternative approach to using empirical transfer functions is to compute the functions directly from a realistic earth model. The potential weakness of such an approach is that generally accepted attenuation models for the crust (frequency range 1 to 10 Hz) are not available. However, two distinct data sets can be used to decide if the attenuation for a given earth model is realistic. A high-frequency constraint on the attenuation model is the observed behavior of peak acceleration versus distance at ranges greater than a few source dimensions. Seed *et al.* (1976) have reviewed the various empirical relationships between peak acceleration and distance. The behavior of most of these functions varies as $R^{-\beta}$ where β ranges from 1.5 to 2.0. For comparison with the simulated accelerograms, an intermediate value of $\beta = 1.75$ was chosen as being reasonably representative of the observational data. A second constraint is the stability of the calculated local magnitude, M_L, as a function of distance. These constraints were applied to four attenuation models. The elastic velocity model is discussed below. The four attenuation values tested were: $Q_\beta = \infty$; 300; 200; and 100, where Q_β is the shear-wave quality factor. In all cases, the attenuation was uniform throughout the model. The value $Q_\beta = \infty$ did not meet the constraints discussed above. However, only a slight

TABLE 1

EARTH STRUCTURE MODEL

Thickness (km)	α (km)	β (km)	ρ (gm/cm^3)
1.4	2.5	1.3	2.2
2.1	4.8	2.8	2.6
4.5	5.9	3.4	2.76
18.0	6.5	3.7	2.8
6.0	7.0	4.0	3.0
∞	8.2	4.7	3.3

amount of attenuation was required in order to bring the transfer functions into good agreement with these constraints.

The velocity model used to calculate the transfer functions is listed in Table 1. This velocity model has been adopted from a profile through the southern California Peninsular Ranges as discussed by Shor and Raitt (1956). The top few kilometers were altered to incorporate a sedimentary structure. The shear-wave velocity in the top layer was set at $V_\beta = 1.3$ km/sec. This velocity corresponds to a very stiff or well-cemented seidment. The model does not incorporate a soft surficial layer with nonlinear properties. If such a layer were included, the effect on the derived attenuation relationship would be to systematically decrease the computed accelerations proportional to the absolute acceleration.

The expense of computing transfer functions for a homogeneous half-space is much less than for the layered model defined above. However, there are several compelling reasons why a half-space model is not appropriate. The work of Heaton and Helmberger (1978) has clearly shown that elastic propagation through a layered earth alters the spectrum of the input pulse, whereas a homogeneous model results in a flat spectrum. Another consideration is initially downward traveling energy. In the homogeneous model, this energy never contributes to the accelerogram. In the simulations discussed below (see Figure 2), the amplitudes are appreciably increased beyond about 60 km by critical reflections from deeper layers. Without the lower

part of the model, it would not be possible to match observations at larger distances. If the simulations are expected to match the observations, a layered earth model must be used.

It is useful to regard the accelerogram recorded at any distance as the convolution (or product in the frequency domain) of three distinct operators

$$ACC(R) = T_{elastic} * Q * Source \tag{1}$$

where $T_{elastic}$ is the purely elastic transfer function for the model discussed above, the Q is the attenuation operator, and source is the time function radiated by the earthquake source. The transfer functions represent the displacement time history at a point on the surface that results from a step dislocation at depth. A primary goal of this section is to select a reasonable Q model that is consistent with observations over the frequency range of interest for modeling strong ground motion. By previously choosing a velocity model based on refraction and reflection surveys in southern California, the velocity model is fixed. Similarly, if real earthquake source-time functions are used, then the frequency content of the source cannot be traded off with the attenuation model in order to match the constraints on $ACC(R)$. Real, nearly pure source functions have been recorded for a few earthquakes. As seen from equation (1), a recorded accelerogram will represent the source-time function if the product of $T_{elastic} * Q$ is a delta function. This condition is approximately true if the accelerogram is recorded at very small epicentral distances (epicentral distance/source depth < 1) and if the source-to-station path is uniform and high Q. These conditions were ideally met for several recordings of an $M_L = 4.8$ earthquake in southern California [Horse Canyon, Peninsular Ranges studied by Kanamori (1976) and Hartzell (1978)]. For this study, the most significant accelerogram was recorded at station Terwilliger, located on hard rock. The epicentral distance for this earthquake ($\Delta = 5.75$ km) was approximately half of the hypocentral depth. Hence, by convolving together the transfer functions computed from the elastic layered earth model discussed above and the Terwilliger accelerograms, accelerograms for a perfectly elastic earth, $Q = \infty$, can be computed for any epicentral distance or source depth. These simulated accelerograms can also be filtered with the instrument response of a Wood-Anderson seismograph, and local magnitudes (M_L) can be computed at each distance (Kanamori and Jennings, 1978). An example of the strike-slip transfer functions for SH energy, computed using the elastic-layered earth model described above, and the simulated accelerograms and Wood-Anderson responses, are shown in Figure 1. The computation of these transfer functions is discussed by Helmberger and Malone (1975). The behavior of the peak acceleration versus distance curve for these simulated accelerograms can be directly compared with the trend of the observational data (Figure 2). This comparison clearly shows that the peak acceleration or zero-period response of the simulated accelerograms, for the purely elastic earth, decays too slowly with distance. In addition, the M_L calculated from the records systematically increases with distance (Figure 3). These two comparisons show that the response at zero period and 1 sec are not in good agreement with the observations.

The complete computation of transfer functions for a given velocity and attenuation model is a rather costly process. In searching for an attenuation model that meets the above discussed constraints, it is desirable to use an approximate but efficient method for incorporating anelasticity. Attenuation can be added to the elastic transfer functions in an approximate manner by convolving the entire elastic response with a single attenuation operator (Carpenter, 1966). Since the peak

acceleration and the maximum excursion of the Wood-Anderson response is controlled primarily by the largest arrival, the appropriate attenuation operator is defined by the travel time of that arrival and a value of Q_β. For a constant Q earth model, this approach adds too much attenuation to the early part of the record and too little to the late part. However, for the point of maximum interest, the technique accurately attenuates the pulse. Two values of Q_β were examined: $Q_\beta = 100$ and 200. It should be emphasized that attenuation in all of the modeling was both linear and uniform throughout the model. The behavior of peak acceleration versus distance for these attenuated transfer functions and the computed M_L, for each simulated accelerogram, are shown in Figure 4. These approximately attenuated transfer

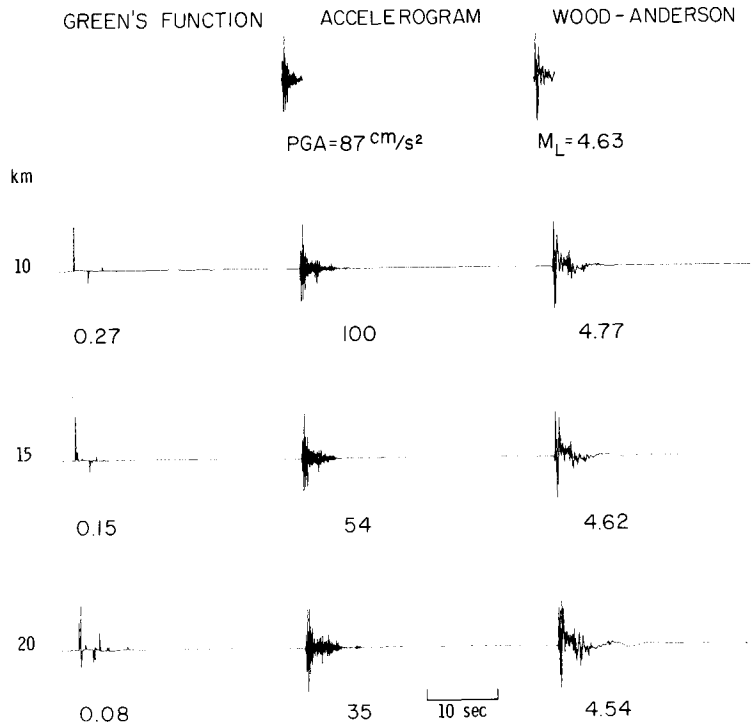

FIG. 1. The Green's functions represent the *SH* displacement time history at a point on the surface of the earth that results from a step dislocation at a depth of 6.5 km. A simulated accelerogram can next be constructed by convolving together these Green's functions with an observational source function. The *first row* shows the observed accelerogram, $M_L = 4.8$, recorded on a hard rock site, that was used in this simulation (see discussion in text). The convolution of the accelerogram with the response of a Wood-Anderson seismograph results in the final seismogram. The local magnitude, M_L, is then calculated from this final record.

functions show much better agreement with the observational constraints and further indicate that fairly high crustal Q_β values are compatible with the observed behavior of peak acceleration and M_L.

By selecting a macroscopic velocity model and using a real earthquake source, the Q operator was bounded with the observations of the behavior of $ACC(R)$. However, the bounds on the Q model are sensitive to the earthquake source function used in the application of equation (1). For instance, if the earthquake source function was enriched in long-period energy, relative to an "average" earthquake of the same magnitude, then Q would have to be reduced in order to obtain the observed decay of peak acceleration. On the other hand, if the source function was

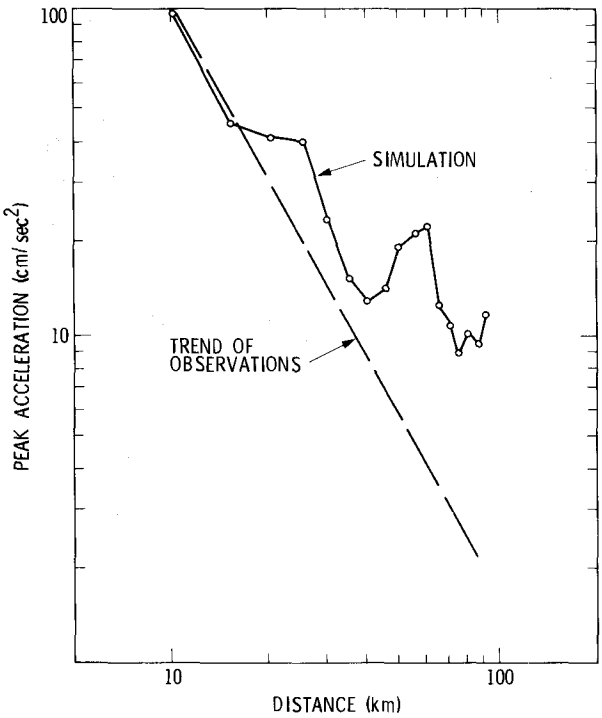

FIG. 2. Comparison of the behavior of peak acceleration versus distance for the simulation ($Q = \infty$) with the trend of the observations, $M_L \sim 4.5$. Note that the simulations have been normalized to 100 cm/sec^2 at an epicentral distance of 10 km.

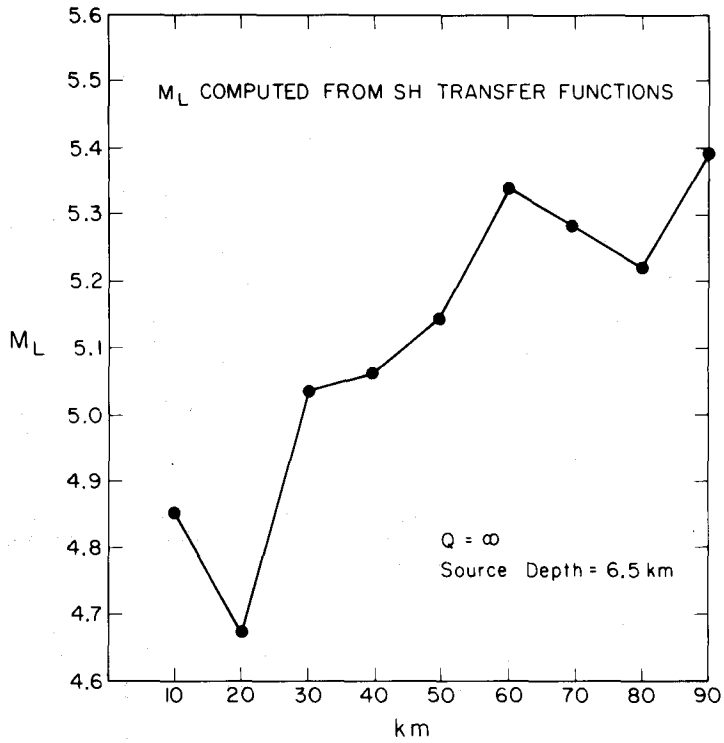

FIG. 3. Computed M_L as a function of distance for the perfectly elastic earth.

enriched in high frequencies, Q would have to be increased so that the computed peak acceleration would not decay too quickly with distance. The Horse Canyon source function was enriched in high-frequency energy (Hartzell, 1978). Hence, the value of $Q_\beta = 100$ to 200 may represent a larger value of Q than would be derived

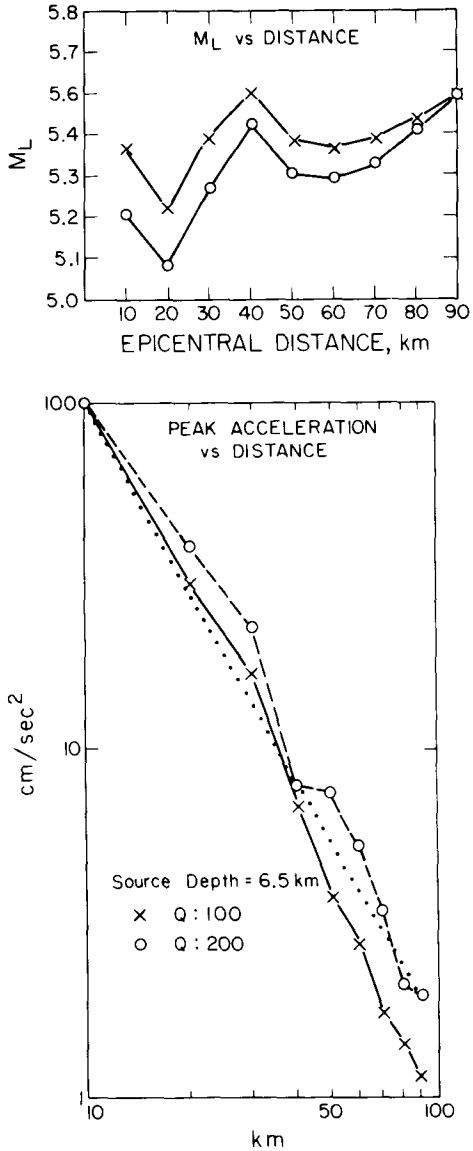

FIG. 4. Behavior of M_L and peak acceleration versus distance for *SH* energy for two values of Q_β. In both figures, peak acceleration has been normalized to 100 cm/sec^2 at 10 km. The dotted line in the *lower figure* is the trend of the observed data (slope $\sim R^{-1.75}$).

from an "average" earthquake source. The behavior with distance of the parameter M_L is not particularly sensitive to the source since the Wood-Anderson instrument filters all input signals with a response that is peaked at 0.8 sec. By comparison with the variable width of the peak acceleration pulse, or its frequency content, the period of the maximum pulse of the Wood-Anderson instrument is fairly stable.

The selection of Q in the model will essentially control how much high-frequency energy released from more distant sections of a fault will arrive at any particular site. Hence, for simulating peak ground acceleration, the Q model must be accurate. The approximately attenuated synthetic accelerograms computed using a uniform crustal Q_β of 100 to 200, are in fairly good agreement with the data. The next step in the process of selecting a Q model is to compute the transfer functions with a more exact technique. Functions for five source depths and 18 distance ranges (Δ = 5 to 90 km) were calculated with $\omega - K$ integration (Apsel, 1979). The $\omega - K$ integration technique correctly introduces the attenuation into the transfer functions. A uniform Q model of $Q_\beta = 300$ and $Q_\alpha = 600$ was selected for testing at this stage of the study. Examples of these transfer functions for one source depth are shown in Figure 5.

Again, the comparison between the simulated peak acceleration and the calculated behavior of M_L, for each depth and distance range, and the observational data must be performed. The simulated peak acceleration versus distance curve, $M_L = 4.5$ to 5.0 (since the source-time function came from an $M_L = 4.8$ event), is shown in Figure 6. The calculated variation of M_L with distance is shown in Figure 7.

In recent studies of M_L, computed from near-field accelerograms, Kanamori (personal communication) has found a systematic dip of ~0.2 units at 20 km in the measured value of M_L. The M_L simulations plotted on Figure 7 show that the computed response for the crustal model is in very good agreement with this observation. The confirmation of trends found in the simulations with observational data strengthens the credibility of the modeling. The combined results suggest that the standard M_L amplitude corrections are slightly in error. As the simulations are for strike-slip faulting, the model results must be extended in future studies to include dip-slip earthquakes.

Matching the zero period and 1-sec response of these transfer functions to the observational data is crucial since the larger strike-slip faults simulated below will be developed by adding together fault elements typified in areal extent and moment by earthquakes with $M_L \sim 5$. The good comparison between the computed transfer functions and observational data indicate that the following simulations should be very realistic. These transfer functions, convolved with real earthquake source functions, will be used in a manner exactly analogous to that described by Hadley and Helmberger (1980) to simulate accelerograms from larger earthquakes.

Source-time functions. In the hybrid simulations discussed in Hadley and Helmberger (1980) and in this study, the term source-time function represents the time history of the energy radiated by an element of the simulated fault. This function represents the convolution of the fault rupture process with a distribution of particle rise times. In an idealized model, rupture across the grid would modulate the radiated function; each azimuth would record a slightly different time history. Inclusion of these effects into the modeling require assumptions on the microbehavior of each fault element. The limited constraints on the high-frequency behavior of the fault surface and the wide range of proposed fault models (e.g., Brune, 1970; Andrews, 1980) restricts the general applicability of a purely deterministic approach. The herein proposed model uses observational data to construct a function that, on the average, describes the energy radiated by a fault element. Neglecting the microeffects of rupture across each element by using an average representation of the source time function implies that the simulations should not display the full dispersion of observed values of peak ground acceleration. However, as the primary

goal of this study is to estimate the mean behavior and not the dispersion, this detail is probably not significant.

In the preceding section, the source-time function used in the verification of the computed transfer functions came from the Horse Canyon earthquake. The moment

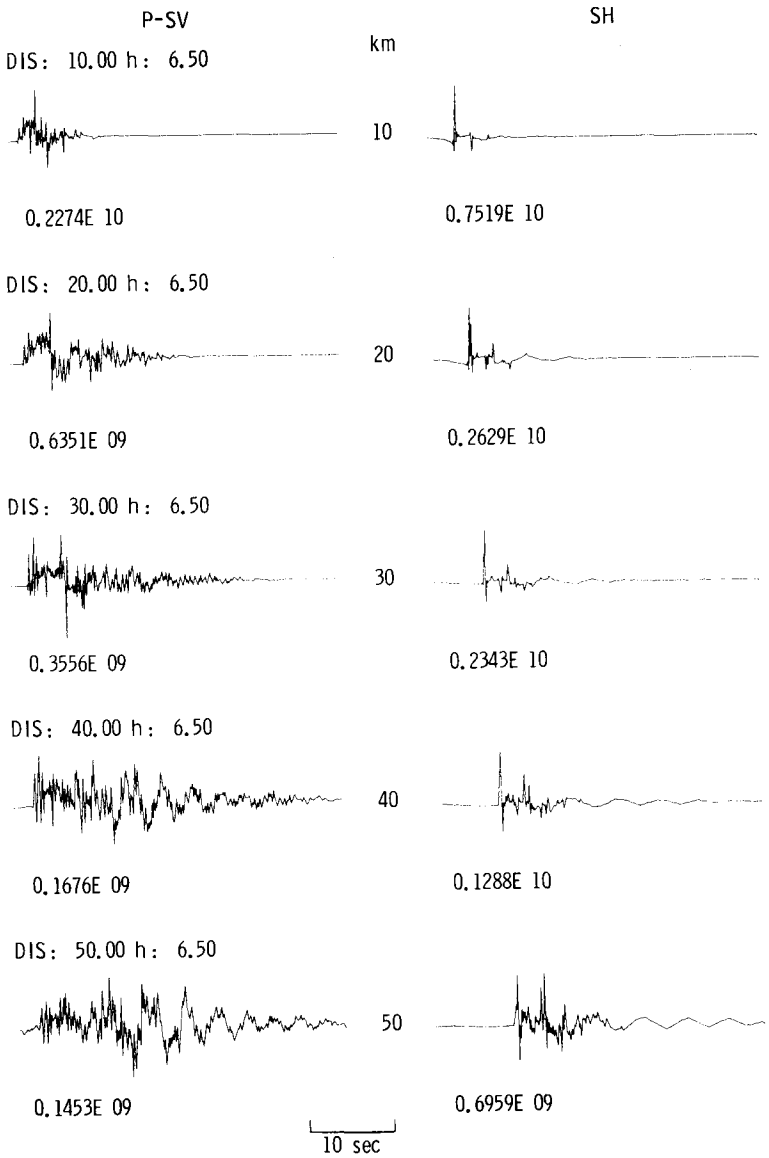

FIG. 5. Examples of the transfer functions computed from the velocity model listed in Table 1 and a uniform, linear $Q_\beta = 300$. The column on the *left* is for *P-SV*, and the column on the *right* is for *SH*. The source depth is 6.5 km.

of this event was $M_0 \sim 3 \times 10^{23}$ dyne-cm (Kanamori, 1976; Hartzell, 1978). In order to reduce the scaling required to simulate larger events, and to use an earthquake source function that is closer in magnitude to the events of interest in this study, source functions from a larger earthquake are desirable. A candidate earthquake for obtaining a good source-time function is the $M_L \sim 5.7$ Coyote Lake earthquake that

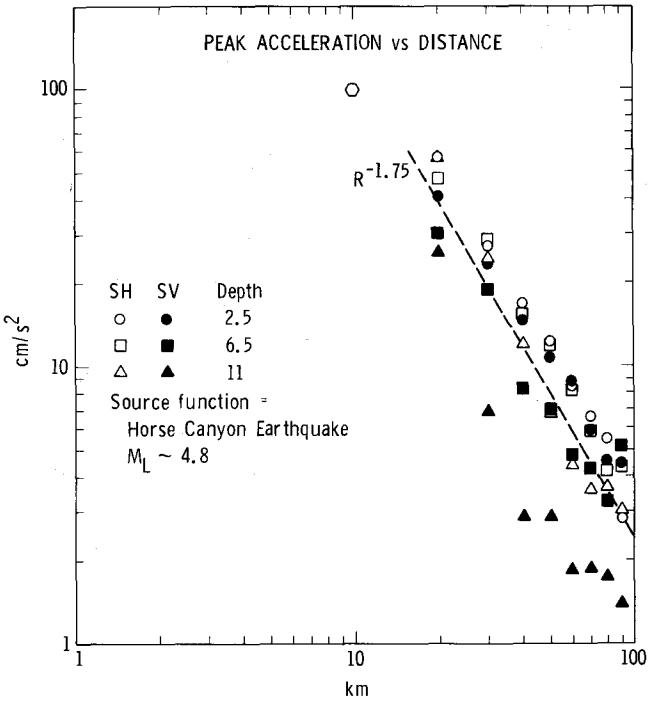

FIG. 6. Computed behavior of peak acceleration versus distance for both *P-SV* and *SH*. An example of the transfer functions used in these calculations is shown in Figure 5. The absolute amplitude of each family of points has been normalized to 100 cm/sec^2 at 10 km.

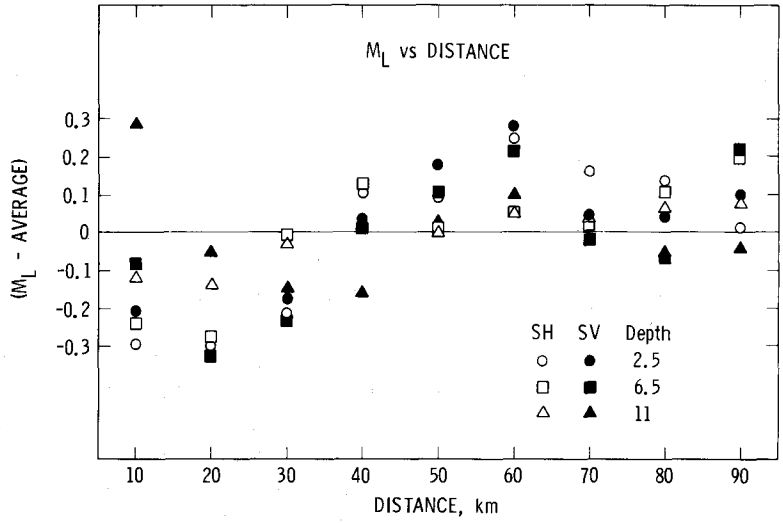

FIG. 7. Computed behavior of M_L versus distance for both *P-SV* and *SH*. An example of the transfer functions used in these calculations is shown in Figure 5. Typical scatter or uncertainty in determining values of real M_L is ±0.2 to 0.3. The mean value for each family of points has been subtracted in order to emphasize ΔM_L.

occurred near Hollister on 6 August 1979. Some of the details of this earthquake have been discussed by Lee *et al.* (1979). This event was well recorded in the near-field by several accelerographs. In particular, Station 6 and Coyote were located within about one source depth of the earthquake. Both stations were located on the approximate projection of the fault plane. From studies of the near-field records,

and from consideration of the locations of the main shock and aftershocks, rupture initiated near Station Coyote and ruptured south toward Station 6. In order to use this event for simulating strong ground motion, the parameters seismic moment and source duration must be estimated. To obtain this information, the tangential velocity pulse from the six near-field stations that recorded this event have been modeled. Using the focal mechanism and location of Lee *et al.* (1979), a moment of 4.5×10^{24} dyne-cm and a source duration of ~1.3 sec results in synthetic seismograms that are in fair agreement with the observations. This moment was obtained by Langston (personal communication) from modeling of teleseismic data, and is in good agreement with the determination by Uhrhammer (1979).

Accelerograms from either Station Coyote or Station 6 approximately meet the criteria discussed above as candidates for the source-time function. An examination of the accelerograms (Figure 8) suggests that these records contain some effects

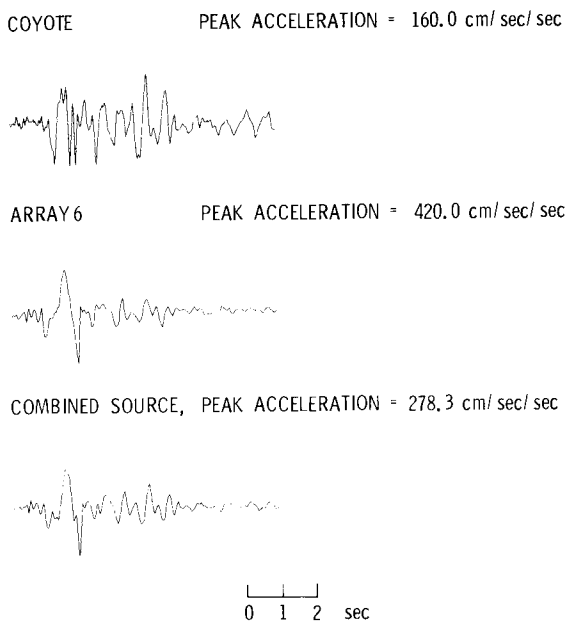

FIG. 8. Coyote, Station 6, and the composite accelerograms.

from local site conditions. A data set recorded on hard rock sites would reduce this contamination. The response spectra, damping = 5 per cent, for Station 6 and Coyote are shown on Figure 9. Comparison of the response spectra over the period range 0.1 to 0.6 sec shows a greater acceleration amplification for Coyote. On the other hand, by normalizing the two records to a common zero-period response, the long-period response (>1 sec) at Station 6 exceeds the response at Coyote. An average or composite source-time function was obtained by aligning the *S*-wave pulses and averaging the records at each time point. The composite time function is shown on Figure 8, and its response spectrum is depicted on Figure 9. This figure shows that the composite source is a good average of the two extreme cases represented by Coyote and Station 6.

The composite source-time function represents the average time history of energy radiated from a section of the fault surface. This implies that the grid size used in the simulation of larger events must be compatible with the observed source duration. The selected grid size of 2 km vertically and 3 km horizontally is approx-

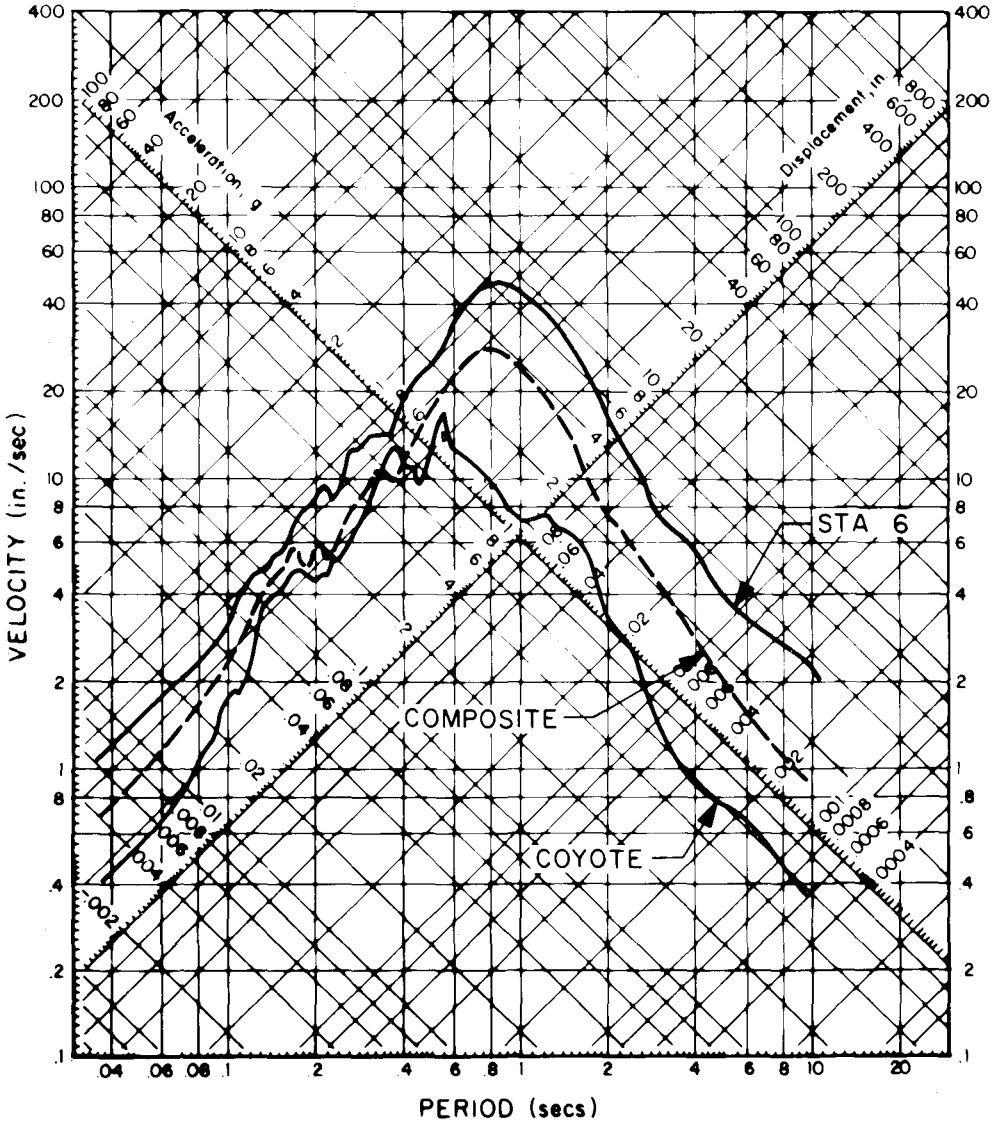

FIG. 9. Response spectra for stations Coyote, Station 6, and the composite accelerogram. All three accelerograms are shown on Figure 8.

imately compatible with the duration of 1.3 sec and a rupture velocity of 90 per cent of the shear-wave velocity. The short duration implies a much smaller source dimension than indicated by the extent of the aftershock sequence (Lee *et al.*, 1979). It is possible that the strong ground motion data represents the effects of localized failure or rupture across an asperity similar to that observed for the Horse Canyon earthquake (Hartzell, 1978).

A final consideration in the adoption and use of the accelerograms from the Coyote Lake earthquake is the effect of attenuation along the path from the hypocenter to Station 6 or Coyote. The transfer functions discussed above explicitly include attenuation. Hence, the use of real accelerograms include intrinsic attenuation twice—once in the real earth and once in the simulation. For the Coyote Lake earthquake geometry, this is equivalent to adding an extra attenuation operation to equation (1), defined by a total path length of ~10 km (hypocenter to the station) and a $Q_\beta = 300$. The effect or significance of this redundant operator is easily estimated by calculating the decrease in amplitude of the high-frequency components of the accelerogram. For instance, the decrease in the amplitude of 5 Hz energy is 2.5 per cent. As this error is an order of magnitude less than the standard deviation of the peak accelerations generated from a range of geometries, as discussed below, the effects of the slightly redundant attenuation operator are insignificant.

Within the last two sections, operators have been developed that describe the crustal response and the average energy radiated from a patch or grid element of a larger fault. The adequacy of the crustal response functions has been tested through comparisons with observations of the behavior of peak acceleration and M_L. The next stage in the modeling of the peak acceleration is to use these functions as elements for simulating a larger earthquake.

Attenuation Relationships for $M \sim 4.5$, 5.5, 6.5, and 7.0

Earthquake ground motions are influenced by source effects, propagation effects, and by site effects. Empirically derived relationships for characterizing ground motion (e.g., peak acceleration) have typically been related to these parameters by simple expressions. These functions use magnitude to represent source effects, distance to represent propagation effects, and site effects are either ignored or separate expressions are derived for each general site condition. For example, peak ground acceleration (PGA) has been expressed in the most general way as

$$PGA(M_S, R) = B(M_S) \cdot (R + C(M_S))^{-\beta} \tag{2}$$

where R is closest distance to the fault trace, B and C are assumed functions of magnitude, M_S, and β controls the far-field ($R >> C$) decay of PGA. This functional form of an attenuation relationship was first proposed by Esteva (1970), and in its general form has been widely used by various investigators (Idriss, 1978). The principal guiding philosophy in selecting the functional form of any equation used to describe data has been that it uses a minimum number of parameters. An arbitrarily selected form cannot, in general, accurately model the phenomenon; instead, it can only represent mathematically the empirical effects of the phenomenon. A major goal of the present study is to evaluate the behavior of peak acceleration in the near-field of large earthquakes. The term $(R + C)^{-\beta}$ simply describes the near-field trend. If $C(M) \equiv 0$ peak acceleration increases without limit as R approaches zero. For $C(M)$ = constant (other than zero), peak acceleration is bounded. Finally, if $C(M)$ increases with magnitude, peak acceleration tends toward saturation as magnitude increases.

The exponent of the assumed attenuation relationship controls the decay of the curve at distances where $R >> C$. With increasing distances, it is commonly observed that seismograms systematically shift to a longer dominant period. In the far-field, the amplitude of the long-period pulse from an earthquake scales with moment. Hence, a reasonable and fairly common assumption (e.g., Esteva, 1970; Donovan,

1973) is that the exponent is either independent or only very weakly dependent on the magnitude. This assumption is also well-supported by a study involving 2900 accelerograms recorded over the distance range 1 to 600 km from nuclear events ranging in yield from 1 to 1200 kt (Murphy and Lahoud, 1969).

The technique used in the following sections to simulate the larger events ($M \sim$ 6.5 and 7.0) is described in Hadley and Helmberger (1980). However, instead of having only 12 accelerograms from one earthquake recorded over the epicentral range 5 to 33 km, a library of effective 360 records has been developed by convolving together source-time functions with the computed crustal response functions. This library represents simulated accelerograms for strike-slip earthquakes for five source depths, (2.5, 4.5, 6.5, 9, and 11 km) and 18 evenly spaced epicentral distances (Δ = 5 to 90 km) and two magnitudes (Horse Canyon and Coyote Lake).

$M \sim$ 4.5 to 5.0. Simulated accelerograms in this magnitude range were computed by convolving together the various crustal response functions discussed above with

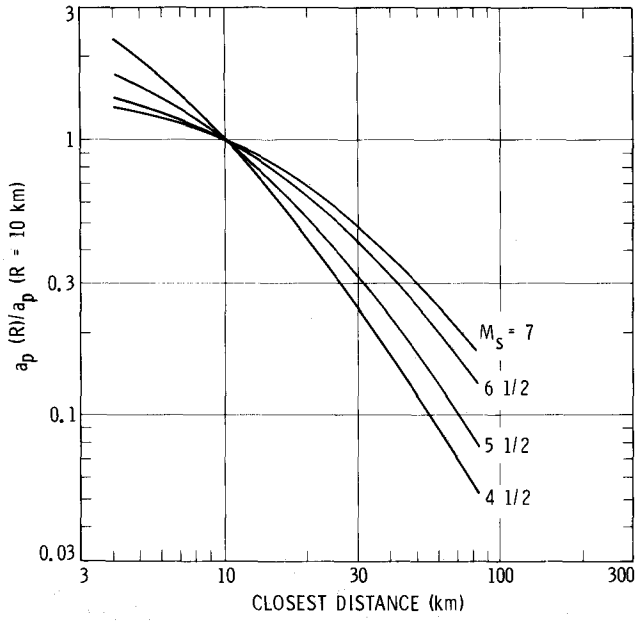

FIG. 10. Summary of normalized attenuation curves derived in this simulation study.

a source function. For eight distances (5, 10, 15, 20, 30, 40, 50, and 70 km) and five source depths, accelerograms for *SV* and *SH* were simulated with the source function from the Horse Canyon earthquake. The simulated peak acceleration data shown on Figure 6 indicates the range of computed values. A simple regression curve of the form $(R + C)^{-1.75}$ was fit to the data. The best-fitting value of C was 6 km and the standard error was 52 per cent. The curve shown in Figure 10, labeled M = 4.5, shows the shape of the derived attenuation relationship. Because the evaluation of the shape of the attenuation relationship is of primary interest in the present study, the curves shown on Figure 10 have been normalized to a common value at 10 km.

$M \sim$ 5.5 to 6.0. The attenuation relationship for earthquakes in this magnitude range was evaluated by convolving the composite Coyote Lake source-time function (M_L = 5.7) with the crustal response functions discussed in the previous sections. Figure 11 shows the behavior of the peak acceleration curve for a source depth of

6.5 km for the Coyote source. Also shown in this figure are the corresponding points for $M \sim 4.5$. Both sets of points have been normalized to 100 cm/sec^2 at an epicentral range of 10 km. It is interesting to note that the points for $M \sim 5.5$ systematically show higher peak accelerations. In addition, the separation between the two sets of points increased with distance. As the crustal response functions used to compute both sets of points are identical, the explanation of this observation must involve the different source functions (Horse Canyon versus Coyote Lake). An obvious explanation is that the composite Coyote Lake source represents a much larger earthquake (the ratio of the moments of these two events is ~15) and the long-period excitation of the structure by this source is correspondingly greater. Diffraction effects from wave propagation through the crustal structure are not as effective

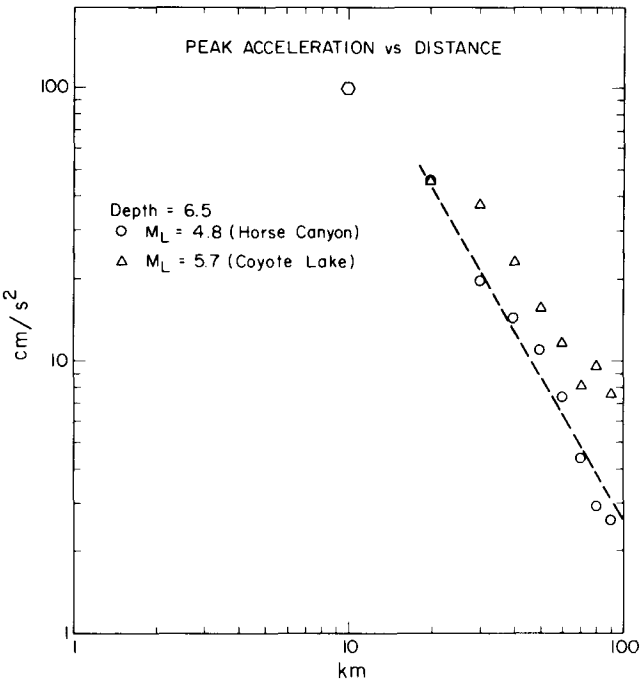

FIG. 11. Peak acceleration versus distance for $M_L = 4.8$ and 5.7. The transfer functions used for each distance are identical. Note that the attenuation relationship for the larger source is distinctly different from the curve computed from the Horse Canyon source, even though both sets of points have been normalized to 100 cm/sec^2 at 10 km. The longer period energy from the larger source interacts with the earth structure such that the decay of peak acceleration at short distances is not as severe as for the higher frequency, smaller earthquakes.

in smoothing long-period pulses (Heaton and Helmberger, 1978) and the effects of energy loss to the medium from intrinsic attenuation is diminished. Hence, the decay of peak acceleration at short distances is not as severe for the larger magnitude source. The curve shown on Figure 10, labeled $M = 5.5$, has been developed exactly as described above for the case $M = 4.5$. The best-fitting value of C was 12 km, and the standard error was 47 per cent.

$M \sim 6.5$. Simulation of an earthquake with physical dimensions larger than either the Horse Canyon or Coyote Lake earthquakes requires a careful definition of the source properties. The Borrego Mountain earthquake of 9 April 1968 has been selected as a model event. The various magnitudes for this event are: $M_S = 6.7$; $m_b = 6.1$; $M_{Pasadena} = 6.4$; M_L (from strong motion records, Kanamori and Jennings,

1978) = 6.9. Following the study of Burdick and Mellman (1976), a moment of 1×10^{26} dyne-cm and fault dimensions of 24 km by 10 km (8×5 grid elements) have been used. The fault dimensions are very comparable with the 1979 Imperial Valley earthquake, M_L (Pasadena) = 6.6. In order to obtain a robust estimate of the mean and standard deviation of the simulated peak accelerations at each distance, four different fault rupture geometries have been examined. These various geometries are shown on Figure 12 and represent the extremes in possible rupture configurations. For the case of bilateral rupture initiating at the closest epicentral distance, geometry 3, accelerograms for rupture initiating at both the top and bottom of the fault have also been simulated. Hence, for each distance, 10 time histories (radial and transverse) and five values of maximum peak acceleration were derived.

The simulation of the rupture front through the grid is described in Hadley and Helmberger (1980). A random number generator is used to select a position within each grid element for the calculation of the travel-time and rupture initiation. This minimizes the introduction of a strong periodicity into the simulations that would result if each grid element were turned on exactly when the rupture front reached the edge of the element. Because of the introduction of a stochastic aspect to the turn-on location in each element, the simulation is composed of a fault that has some patches breaking nearly simultaneously and others that are distributed. In effect, the code partially captures the physics of asperities distributed randomly over the fault plane. However, by changing the seed in the random number generator, the asperities will be distributed differently and the simulated earthquake will exhibit slightly different characteristics. Hence, a single calculation of time histories and peak accelerations for one rupture station geometry and one seed in the random number generator is not sufficient to define a robust estimate of the attenuation relationship. In order to examine the overall stability of the mean for the different rupture geometries, over the distance range 5 to 70 km, the seed in the number generator was changed and the entire simulation for all rupture geometries at all distances was recomputed. For each distance, the average difference of the mean for the first run (five values) compared to the mean for the two runs, was less than 3 per cent. From this, it is concluded that the mean from one complete run is a good representation of the true mean. Equation (1) was combined with the 80 simulated peak accelerations (8 distances, 10 values of peak acceleration) in a standard regression. Figure 13 shows the simulated peak acceleration points and the derived regression line. As C was increased from 0 km, the standard error of the best-fitting line decreased from 156 to 24 per cent at $C = 22$ km. The standard error is fairly flat over the range 20 km $\leqq C \leqq$ 30 km. The standard error for this magnitude range is less than found for $M \sim 5.5$. For the smaller events, the larger range of accelerations resulted from the effects of source depth, i.e., peak accelerations from shallow and deep sources were combined in the regression. For the large distributed faults simulated for $M \sim 6.5$, the effects of source depth are somewhat homogenized and the standard error reflects the effects of rupture geometry and randomness in the rupture process. As discussed in Hadley and Helmberger (1980), the absolute position of this curve is sensitive to the rupture velocity or dynamic similarity conditions. The normalized results of this simulation are summarized on Figure 10.

$M \sim 7.0$. As with the simulation of the $M \sim 6.5$ earthquake, the physical dimensions of the $M \sim 7.0$ event must be carefully selected. This selection has been based on the data discussed by Slemmons (1977). The necessary parameters to be extracted from these data are fault length and displacement. The regressions

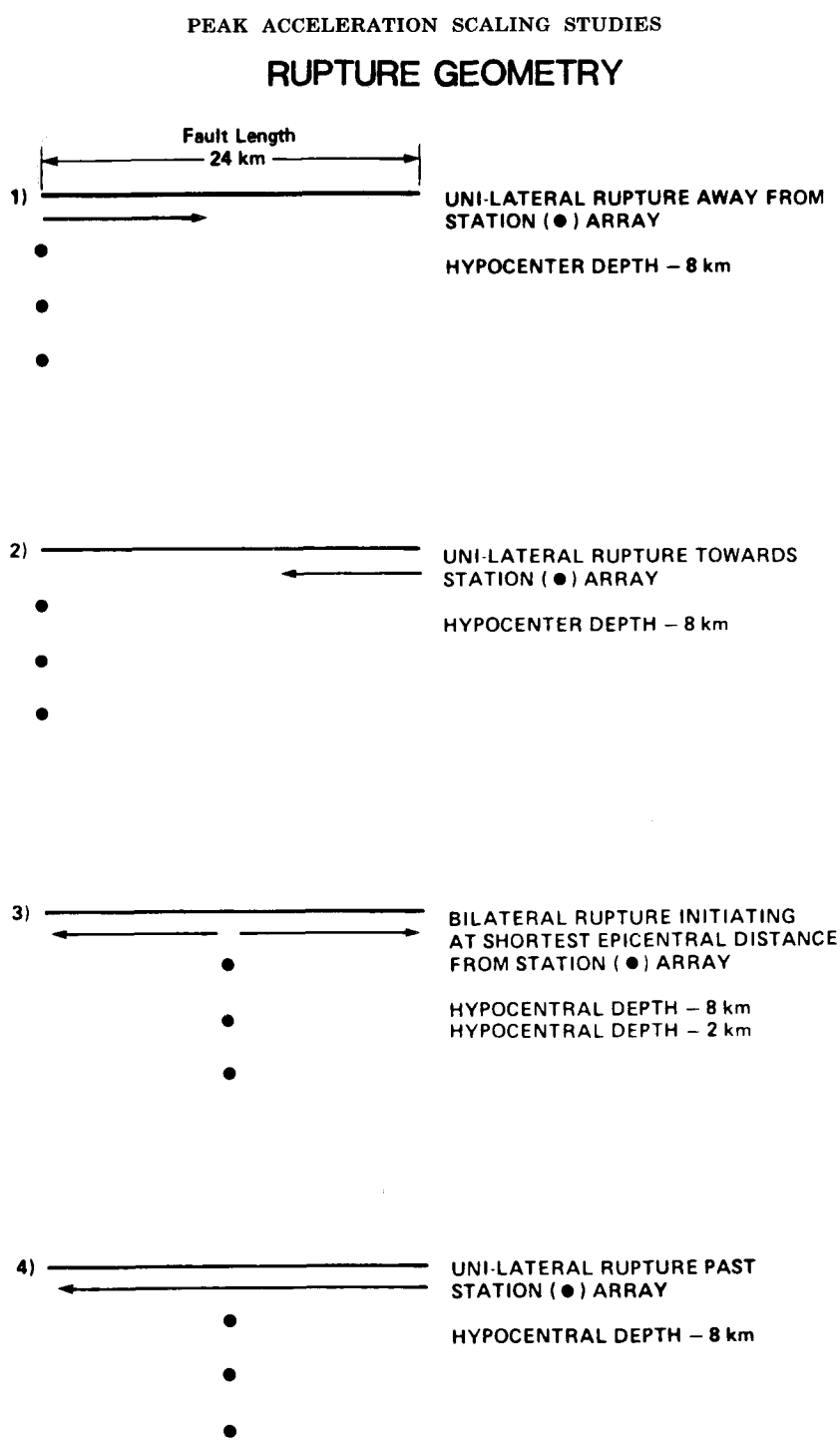

FIG. 12. Rupture geometries used in the simulation studies.

discussed by Slemmons are in the form $M = a + b \log x$. However, given M_S, the fault parameters must be selected ($\log x = a + b M_S$). Therefore, using the data discussed by Slemmons, a new regression curves for strike-slip earthquakes, for fault length, and fault displacement have been derived. For $M_S = 7.0$, the appropriate fault length was computed to be 45 km (15 by 5 grid elements). The derived ratio of

the fault displacement ($M_S = 7.0$ to $M_S = 6.5$) was 1.55 to 2.45 for the maximum and average curves, respectively. The moment was computed from the product of the ratios of fault length, fault displacement, and moment of the $M = 6.5$ event: $M_0 = 3.8 \times 10^{26}$ dyne-cm. As with the simulations for $M_S = 6.5$, the rupture geometries shown in Figure 12 were used for simulating $M_S = 7.0$. The regression curve that best fits the simulated peak accelerations is shown on Figure 10. As C was increased

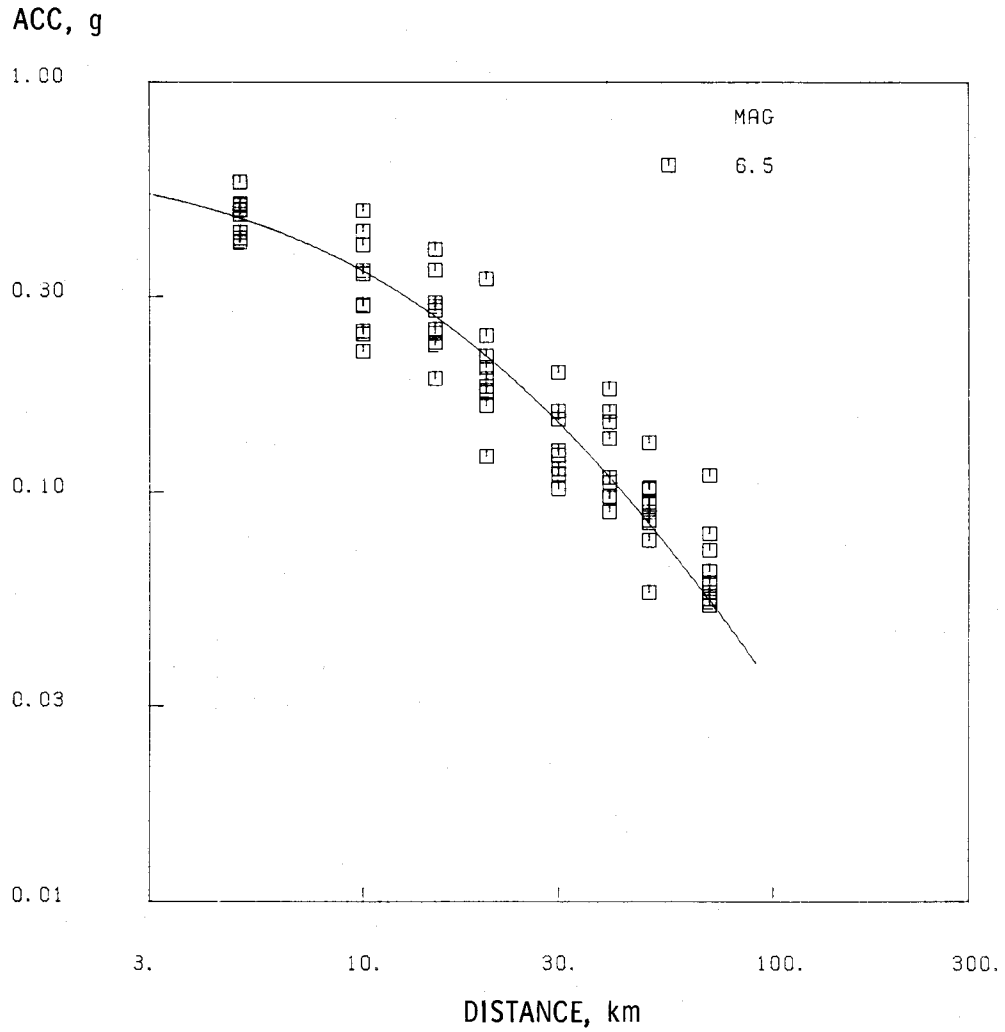

FIG. 13. Simulated peak acceleration points for the magnitude $M = 6.5$.

from 0 km, the standard error decreased from 252 to 24 per cent at $C = 36$ km. The standard error is fairly flat over the range $34 \leqq C \leqq 50$.

DISCUSSION

Figure 10 shows the summary of the normalized attenuation curves developed from average peak accelerations at eight distances and four magnitudes. Each curve represents the end result of many physical processes that include the source-time function, various rupture geometries, propagation through a realistic crustal struc-

ture, and absorption by intrinsic attenuation. The trend toward flattening or saturation of the attenuation curve with increasing magnitude is obvious in the summary (Figure 10). The trend toward saturation is well known for other peak parameters in seismology. Classic examples include M_S, m_b, and M_L as measured against moment.

Several physical arguments can be advanced to describe why peak ground acceleration should saturate. The adequacy of these arguments and the results of these simulation studies must be tested against observations. In this study, accelerograms from smaller earthquakes are superposed to simulate a large event. The longer period components of each contributing accelerogram will add together in phase, whereas the high-frequency components will have essentially random phase. Hence, with increasing magnitude the long-period component of the accelerogram should increase. Diffraction effects from wave propagation through the crustal structure are not as effective in smoothing or reducing the amplitude of longer period pulses (see Heaton and Helmberger, 1978), and the effects of energy loss to the medium from intrinsic attenuation are diminished. These factors should lead to an attenuation curve that is less severe for larger magnitude earthquakes.

For a long and narrow strike-slip fault, a second physical constraint also leads to the saturation of peak ground acceleration. Each element of the fault contributes to the observed accelerogram with amplitudes that vary as $\sim R^{-1.75}$. The maximum contributions to the final accelerogram are, therefore, derived from the section of the fault that is closest to the station. Sections of the fault that are two or more times further from the accelerograph than the closest fault elements contribute very little to the final record. This consideration suggests that at a given distance, peak ground acceleration is sensitive to the dimensions of faulting, with a characteristic length defined by the fault-station separation. Saturation of peak ground acceleration should be most observable for strike-slip faults where the width of the fault does not increase with magnitude.

A recent regression analyses of near-field peak ground acceleration data by Campbell (1981) is ideally suited for testing trends derived in this study. The functional form of the regression curve used by Campbell is

$$PGA = a\ EXP(bM)(R + C_1\ EXP(C_2M))^{-\ d}. \tag{3}$$

The data set used included 229 values of horizontal acceleration recorded from 27 earthquakes ranging in magnitude from 5.0 to 7.7. The investigation involved two primary analyses. In the first study, all coefficients of equation (3) were adjusted to best fit the observations. Because the data set was truncated at a distance of 50 km, strong tradeoffs exist between the far-field behavior (d) and the influence of magnitude saturation [C_1 exp(C_2M)]. Summary results from the unconstrained model are listed in Table 2. The constrained regression study imposed two restrictions. After analysis of additional data and review of other studies, the parameter d was fixed at 1.75 (the same value as used in this study). A second constraint was derived from a physical consideration. Particle acceleration near the rupture surface should be controlled by the local properties of the rocks and not by the overall rupture dimensions (Brune, 1970; Hanks and Johnson, 1976; Hanks and McGuire, 1981). This constraint was imposed by assuming $C_2 = b/d$. This last constraint effectively assumes a model of saturation of peak ground acceleration. However, the magnitude of the saturated value is not constrained. The model space clearly includes solutions with only slight magnitude dependence and very large values of

near-field acceleration. The summary values for the parameter C [i.e., $C_1 \exp(C_2 M)$] from the constrained model and the results from this study are listed in Table 2.

An examination of Table 2 shows a consistent magnitude dependence for the parameter C. Because of the assumed far-field behavior of $R^{-1.75}$ used in this study, column 2 of Table 2, from the constrained analysis, is most appropriate for direct comparison with the results from this study. Both observations and simulations

TABLE 2

BEHAVIOR OF C FROM SIMULATIONS AND OBSERVATIONS

Magnitude	$C(M)$ (km)		
	Unconstrained*	Constrained*	Simulation
4.5	1	4	6
5.5	3	8	12
6.5	6	17	22
7.0	8	25	36

* From Campbell (1981).

show a uniform increase in C with magnitude. The observational results are systematically 30 per cent smaller than the simulated values. In part, this may reflect the inclusion of large, dip-slip events in the regression analysis. This study has been restricted to the more sensitive case of long and narrow strike-slip faults. From this comparison, we conclude that the trends derived from the simulations are in good agreement with observations.

This modeling study has not investigated the effects of source orientation and crustal structure on the derived simulations. These effects may alter the shape of the scaling curves. Application of these results to geometries and crustal structure conditions significantly different than those used in this study should be done with caution.

ACKNOWLEDGMENTS

The authors thank an anonymous reviewer for comments that improved the manuscript. This research was supported by the U.S. Geological Survey under Contract 14-08-0001-19131, 14-08-0001-19835, and by Southern California Edison.

The views and conclusions contained in this document are those of the authors and should not be interpreted as necessarily representing the official policies, either expressed or implied, of the U.S. Government.

REFERENCES

Andrews, D. J. (1980). A stochastic fault model 1. Static case, *J. Geophys. Res.* **85,** 3867–3577.

Apsel, R. J. (1979). Dynamic Green's functions for layered media and applications to boundary-value problems, *Ph.D. Thesis,* University of California at San Diego, La Jolla, 349 pp.

Brune, J. N. (1970). Tectonic stress and the spectra of seismic shear waves from earthquakes, *J. Geophys. Res.* **75,** 4997–5009.

Burdick, L. J. (1977). Broad-band seismic studies of body waves, *Ph.D. Thesis,* California Institute of Technology, Pasadena, 151 pp.

Burdick, L. J. and G. R. Mellman (1976). Inversion of the body waves from the Borrego Mountain earthquake to the source mechanism, *Bull. Seism. Soc. Am.* **66,** 1485–1499.

Campbell, K. W. (1981). Near-source attenuation of peak horizontal acceleration, *Bull. Seism. Soc. Am.* **71,** 2039–2070.

Carpenter, E. W. (1966). Absorption of elastic waves—An operator for a constant Q mechanism, United Kingdom Atomic Energy Authority, AWRE Report No. 0-43/66, 16 pp.

Donovan, N. C. (1973). A statistical evaluation of strong motion data including the February 9, 1971 San Fernando earthquake, *Proc. 5th World Conference on Earthquake Engineering,* Rome, 1, 1252–1261.

Esteva, L. (1970). Seismic risk and seismic design decision, in *Seismic Design for Nuclear Power Plants*, R. J. Hansen, Editor, MIT Press, Cambridge, Massachusetts, 142–182.

Hadley, D. M. and D. V. Helmberger (1980). Simulation of strong ground motions, *Bull. Seism. Soc. Am.* **70,** 617–630.

Hanks, T. C. and D. A. Johnson (1976). Geophysical assessment of peak accelerations, *Bull. Seism. Soc. Am.* **66,** 959–968.

Hanks, T. C. and R. K. McGuire (1981). The character of high frequency strong ground motion, *Bull. Seism. Soc. Am.* **71,** 2071–2096.

Hartzell, S. H. (1978). Interpretation of earthquake strong ground motion and implications for earthquake mechanism, *Ph.D. Dissertation*, University of California, San Diego, La Jolla, 269 pp.

Heaton, T. H. and D. V. Helmberger (1978). Predictability of strong ground motion in the Imperial Valley: modeling the $M = 4.9$, November 4, 1976 Brawley earthquake, *Bull. Seism. Soc. Am.* **68,** 31–48.

Helmberger, D. V. and S. D. Malone (1975). Modeling local earthquakes as shear dislocations in a layered half space, *J. Geophys. Res.* **80,** 4881–4888.

Idriss, I. M. (1978). Characteristics of earthquake ground motions, presented at: Specialty Conference on Earthquake Engineering and Soil Dynamics, ASCE, Pasadena, California, 115 pp.

Kanamori, H. (1976). August 2, 1975 Horse Canyon earthquake, in *U.S. Geological Survey Open-File Report on Earthquake Prediction Studies in Southern California*, October 1975–September 1976.

Kanamori, H. (1979). A semi-empirical approach to prediction of long period ground motions from great earthquakes, *Bull. Seism. Soc. Am.* **69,** 1645–1670.

Kanamori, H. and P. C. Jennings (1978). Determination of local magnitude, M_L, from strong-motion accelerograms, *Bull. Seism. Soc. Am.* **68,** 471–485.

Langston, C. A. (1978). The February 9, 1971 San Fernando earthquake: a study of source finiteness in teleseismic body waves, *Bull. Seism. Soc. Am.* **68,** 1–30.

Lee, W. H. K., D. G. Herd, V. Cagnetti, W. J. Bakun, and A. Rapport (1979). A preliminary study of the Coyote Lake earthquake of August 6, 1979 and its major aftershocks, *U.S. Geol. Open-File Rept. 79-1621.*

Murphy, J. R. and J. A. Lahoud (1969). Analysis of seismic peak amplitudes from underground nuclear explosions, *Bull. Seism. Soc. Am.* **59,** 2325–2341.

Seed, H. B., R. Murarka, J. Lysmer, and I. M. Idriss (1976). Relationships of maximum accelerations, maximum velocity, distance from source and local site conditions for moderately strong earthquakes, *Bull. Seism. Soc. Am.* **66,** 1323–1342.

Shor, G. G. and R. W. Raitt (1956). Seismic studies in the Southern California continental borderlands, International Geological Congress, 20th, Mexico, Tradajos Section 9, t. 2, 243–259.

Slemmons, D. B. (1977). State-of-the-art for assessing earthquake hazards in the United States, Report 6, University of Nevada, Reno, 166.

Uhrhammer, R. A. (1979). Observations of the Coyote Lake earthquake sequence of August 1979, *Bull. Seism. Soc. Am.* **70,** 559–570.

SIERRA GEOPHYSICS, INC.
15446 BELL-RED ROAD, SUITE 400
REDMOND, WASHINGTON 98052 (D.M.H.)

SEISMOLOGICAL LABORATORY
CALIFORNIA INSTITUTE OF TECHNOLOGY
PASADENA, CALIFORNIA 91125 (D.V.H.)

GEOLOGICAL RESEARCH DIVISION
SCRIPPS INSTITUTE OF OCEANOGRAPHY
UNIVERSITY OF CALIFORNIA, SAN DIEGO
LA JOLLA, CALIFORNIA 92093 (J.A.O.)

Manuscript received 31 March 1981